Impact of tip curvature and edge rounding on the plasmonic properties of gold nanorods and their silver-coated counterparts

Charles Vernier, Hervé Portalès

Impact of tip curvature and edge rounding on the plasmonic properties of gold nanorods and their silver-coated counterparts

Charles Vernier[1] and Hervé Portalès[1]
Sorbonne Université, CNRS, MONARIS, UMR 8233, 75005 Paris, France

(*Electronic mail: herve.portales@sorbonne-universite.fr)

(Dated: 20 September 2024)

Colloidal solutions of gold nanorods and silver-coated gold nanorods were prepared. The seeded growth synthesis protocols were improved by adding a flocculation purification step. The resulting populations of pure gold nanorods and Au@Ag core-shell cuboids were characterized by very low dispersion in size and shape. UV-vis-near-infrared absorption measurements were performed on several batches of well-calibrated nano-objects, supported by calculations based on the discrete dipole approximation, allowed to highlight the impact of various morphological features on the optical response. In addition to the well-known effect of the nanorod aspect ratio on the shift of the longitudinal surface plasmon resonance mode, special attention was paid to changing either the rounding of the nanorod end-caps or that of the edges of the coating silver shell. Nanorods and cuboids were modeled as superellipsoids. This approach enabled us to model precisely their complex shapes using just a few simple parameters and analyze the evolution of their extinction spectra as a function of the rounding of their tips and edges. Such nano-objects are widely used for various applications in fields such as biomedical, biosensing, or surface-enhanced Raman spectroscopy, thus making it crucial to precisely assess the impact of each morphological feature for optimizing their performance.

I. INTRODUCTION

The preparation and characterization of gold nanorods (AuNRs) have received a great deal of attention in recent decades because of their rich plasmonic properties, which make them ideal candidates for various applications, particularly in the biological and biomedical fields.[1–4] The optical response of AuNRs involves two localized surface plasmon resonances (LSPRs) associated with the collective oscillation of conduction electrons, either perpendicular or parallel to the AuNR major axis. These two resonance modes are referred to as the transverse and longitudinal LSPR modes, respectively. One outstanding feature of AuNRs is that the wavelength of their longitudinal LSPR mode can be synthetically tuned within the visible and near-infrared (NIR) spectral regions by tailoring their aspect ratio. Actually, it trends out that a linear relationship was found between the wavelength of the longitudinal LSPR mode and the mean aspect ratio of AuNRs.[1,5,6] It has also been shown that the position of the longitudinal LSPR band can be significantly modified by tuning the curvature of the AuNR tip, even forming anisotropic nanoparticles with a dumbbell-like structure.[7] Considerable effort has therefore been devoted to optimizing AuNR synthesis methods to make them more scalable and reliable, enabling fairly fine control of nanorod dimensions and morphology while improving characterization methods.[8,9]

Another possible approach to obtain nanoparticles with a well-defined morphology and optical response is to coat presynthesized AuNRs with another compound. Compared to single-component AuNRs, bimetallic nanorods have even more intriguing physicochemical properties because of the potentially enhanced functionalities offered by the synergistic interactions among different components.[3,10] For example, coating AuNRs with a silver shell reduces the overall plasmonic linewidth by around 20% by modifying the linear relationship between resonance wavelength and nanorod aspect ratio, and reducing the inhomogeneous LSPR broadening of these nanostructures.[11] This so-called "plasmonic focusing" effect provides a simple method for producing plasmonic nanostructures with high-quality factors and a tunable LSPR wavelength over a wide spectral range. These optical properties, combined with the presence on the shell surface of corners and edges, make these silver-coated AuNRs ideal candidates for application in surface-enhanced Raman spectroscopy (SERS).[12–14] Indeed, higher enhancement factors are expected for silver with respect to gold as silver presents stronger plasmon resonances. In addition, the presence of edges and corners on the surface of Au@Ag core-shell nanoparticles, inherent to their cuboidal morphology observed for sufficient silver overgrowth,[15] should also contribute to the enhancement of their SERS activity. A comparison of the SERS efficiencies from self-assembled monolayers of gold-core silver-shell plasmonic nanoparticles with either cuboidal or dumbbell-like shapes revealed that the self-assembled cuboids exhibited a better SERS response.[16] This was attributed to their more uniform packing and efficient generation of electromagnetic hot spots. In addition, it is noteworthy that innovative systems consisting of Raman-active molecules entrapped between a gold core and a silver shell in uniform silver-coated AuNRs have shown a higher SERS response than that of molecules located on the surface of the core-shell nanorods.[17] All these observations make bimetallic cuboids a promising choice for sensing and imaging applications.

Determining the morphological characteristics of AuNRs and their silver-coated counterparts requires direct observation using transmission electron microscopy (TEM) and UV-vis-NIR absorption spectroscopy.[9,18] These two techniques are complementary in such characterization, and their mutual use should make it possible to correlate the spectroscopic response with the morphological parameters of nanostructures. Establishing such a correlation also requires parallel numerical simulations aimed at facilitating the attribution of var-

ious optical features to try to understand its evolution as a function of that of particle morphology.[19] For particles with shapes more complex than spherical or spheroid, various numerical methods were used to calculate their optical response, such as the discrete dipole approximation (DDA), the T-matrix method, finite-difference time-domain (FTDT) simulations, as well as boundary or finite element methods.[20,21] Among these methods, we already proved the DDA method as being successful for simulating the extinction spectra of triangular silver nanoprisms,[22] metal nanoparticles with various crystallinity-related morphologies,[23] spherical metal nanoparticles assembled in close-packed planar arrays,[24] Au@Ag core-shell nanoparticles,[25] and silver rounded nanocubes.[26]

In addition, the DDA method has already been used to analyze the optical properties of AuNRs, in particular their dependence on size, aspect ratio, and end-cap shape.[27–29] In this context, AuNRs have previously been modeled by targets with simple shapes, such as cylindrical, rectangular parallelepipedal, or prolate spheroidal, but which differ substantially from commonly observed AuNR shapes. Other DDA targets, such as cylinders with spherical or ellipsoidal caps, turned out to have shapes much closer to those of real AuNRs, while involving many different parameters. Applying such DDA targets to modeling bimetallic nanorods with a core-shell structure is an even more tedious task, with twice as many parameters to use. Therefore, it is interesting to simplify the target modeling a bit, while remaining faithful to the actual shape of the nanorods to be simulated.

In this work, the impact of tip curvature on the optical response of AuNRs is highlighted. The shape of AuNRs is modified so as to adjust only the curvature of their tip, without involving any deeper change in morphology that would give rise to dumbbell-shaped particles, for instance. In parallel with the UV-vis-NIR absorption measurements, numerical calculations based on the DDA method were carried out, assimilating the nanorods to superellipsoids. This approach makes it possible to accurately model the dimensions and rounded shape of the synthesized nanorods using four fitting parameters: length, width, and two other parameters that define the curvature of the transverse cross-section and tips. Through these measurements and simulations, we observe a redshift of the longitudinal LSPR mode band as the aspect ratio of AuNRs increases. This behavior is in accordance with that observed in previous studies based on the DDA method using different modeling targets.[28,29] Although smaller in scale than the drastic effect of the change in aspect ratio, the position of the LSPR band, nevertheless, remains quite sensitive to the curvature of the nanorod tip. Our DDA calculations show that rounding the tip results in a blueshift of this band by several tens of nanometers. Furthermore, we extend this study to silver-coated AuNRs and show that the use of a superellipsoid-shaped DDA target is also well suited to the simulation of these bimetallic core-shell nano-objects for different silver shell thicknesses and morphologies. The measured absorption spectra were compared with calculated ones, pointing out the increasing contribution of silver to the overall optical response of the core-shell cuboids for increasing silver shell thickness. The influence of the thickness and edge rounding of the silver shell on the emergence of additional plasmon modes and the resulting change in the profile of the spectrum are discussed.

II. EXPERIMENTAL SECTION

To carry out the syntheses described below, all the chemicals were used as received: Hydrogen tetrachloroaurate trihydrate ($HAuCl_4$, $3H_2O$, Sigma-Aldrich, $\geq$99.9%), silver nitrate ($AgNO_3$, Johnson Matthey, 99%), sodium borohydride ($NaBH_4$, Acros Organics, 99%), cetyltrimethylammonium bromide (CTAB, Sigma-Aldrich, $\geq$98%, lot number 102642390), cetyltrimethylammonium chloride 25 wt.-% in water (CTAC, Sigma-Aldrich), benzyldimethylhexadecylammonium chloride (BDAC, Sigma-Aldrich, 97%), sodium oleate (NaOL, TCI, 97%), anhydrous citric acid (Sigma-Aldrich, $\geq$99.5%), L-ascorbic acid (Sigma-Aldrich, 99%), and hydrochloric acid (HCl, 37 wt.-% in water, Carlo Erba). Milli-Q water was used in every synthesis and solutions (resistivity of 18.2 MΩ cm at room temperature).

A. Single-crystal AuNRs

The synthetical protocol followed for the seeded growth of colloidal AuNRs was developed by Ye et al.[8] This protocol, which uses a binary surfactant mixture of cetyltrimethylammonium bromide (CTAB) and sodium oleate (NaOL), enabled us to synthesize single-crystal (SC) AuNRs with different aspect ratios but identical tip morphology. The purification of SC AuNR populations was achieved by flocculation, a shape and size selection process based on the surfactant micelle induced depletion interaction between colloidal particles.[30] AuNRs with larger interparticle contact area form flocculates and can thus be separated from nanoparticles of unwanted shape and size.

1. Synthesis of SC AuNR seeds

364 mg of CTAB were dissolved in 9.75 ml of water in a 50 ml plastic vial. 250 μl of $HAuCl_4$ (10 mM) were added and the solution took a yellow/orange color. 600 μl of freshly made $NaBH_4$ (10 mM) were then added in one stroke under vigorous stirring. The seed solution was vigorously stirred for 2 min then the stirring was stopped and the solution was kept undisturbed for 30 min. At this point, the solution was brown. Seeds solution kept at 28°C would be stable for a couple days before turning pink/red.

2. Synthesis of SC AuNRs

720 mg of CTAB and 89 mg of NaOL were dissolved in 36 ml of water in a 50 ml plastic vial. Dissolution was complete after leaving the closed vial in a water bath at 50°C for a few minutes, followed by gentle manual shaking. The

mixture was then allowed to cool down in a water bath at 30°C. 2.1 ml of freshly made $AgNO_3$ solution (4 mM) were then added. The solution was kept undisturbed for 15 min. Then, 2 ml of $HAuCl_4$ (10 mM) were added and the solution was left under medium stirring for 90 min. The solution took a yellow/orange color and turned transparent after around 15 min due to the reduction of Au^{3+} to Au^{+} by NaOL. 120 μl of 37% HCl were added under slow speed stirring for 15 min. 100 μl of ascorbic acid (64 mM) were added under strong stirring for 30 s, followed by the addition of 40 μl of seeds under strong stirring for 30 s. The solution was then left undisturbed for 12 h at 30°C. The solution was then centrifuged at 5500 g for 45 min and the supernatant was carefully removed. The precipitate was redispersed in 3 ml of CTAB (2.5 mM) and centrifuged at 5500 g for 20 min. The supernatant was removed and replaced by 1.5 ml of CTAB (1 mM). 5 μl of this concentrated stock solution diluted to 1 ml in CTAB (1 mM) had an absorbance of 0.5 at the maximum of the longitudinal LSPR band. The longitudinal plasmon band was centered at 855 nm with a FWHM of 106 nm or 179 meV, indicating a narrow size dispersion of the AuNR population. A shoulder at 560 nm indicates the presence of by-products, such as nanocubes or nanospheres, most of which were removed by a purification step described below.

3. Purification step of SC AuNRs

600 μl of the concentrated SC AuNR solution were mixed with 300 μl of BDAC (480 mM) in a 2 ml Eppendorf tube and left undisturbed for 1 h in an oven at 35°C. The purple/pink supernatant (containing mostly nanocubes and nanospheres) as well as some AuNRs was transferred to another Eppendorf tube, and the black precipitate (containing mostly AuNRs) was redispersed in 1 ml of CTAB (10 mM). The purified AuNRs were centrifuged at 12500 g for 3 min and redispersed, in 1 ml CTAB (2.5 mM). The purified AuNRs were then centrifuged at 12500 g for 3 min and redispersed in 500 μl CTAB (1 mM). 5 μl of this concentrated purified AuNR solution diluted to 1 ml in CTAB (1 mM) had an absorbance of 0.45 at the maximum of the longitudinal LSPR band. The shoulder at 560 nm on an extinction spectrum of the purified solution almost disappears after purification, indicating an increase of the percentage of AuNRs after purification. We estimate that the morphological yield of AuNRs was improved from around 85%, before purification, to over 97%, after purification. A 50 μl aliquot of this solution was kept separately for TEM and absorption measurements on AuNRs without silver shells. The remaining 450 μl were used to make AuNR@Ag nanoparticles. Since the silver shell growth takes place in a CTAC solution, AuNRs were first transferred from CTAB to CTAC. The purified AuNR solution was therefore centrifuged six times at 12500 g for 3 min and redispersed in 1 ml of CTAC (10 mM) each time, except the last time where it was redispersed in around 500 μl of CTAC (1 mM), so that 5 μl of the purified AuNR solution in CTAC diluted to 1 ml in CTAC (1 mM) had an absorbance of 0.35 at the maximum of the longitudinal LSPR band.

B. Pentatwinned AuNRs

In parallel to SC AuNR samples, pentatwinned (PT) AuNRs were synthesized using another protocol also based on the seeded growth of colloidal AuNRs. The protocol steps are briefly described below.[31]

1. Synthesis of PT AuNR seeds

9.6 mg of citric acid, 660 μl of CTAC (25 wt.-% in water), and 250 μl of $HAuCl_4$ (10 mM) were added to 9 ml of water. 250 μl of freshly made $NaBH_4$ (25 mM) were added in one stroke under vigorous stirring. The solution turned brown and was vigorously stirred for 2 min at room temperature. The solution was then kept in an 80°C oven for two hours, after which the solution had turned red, indicating that the seeds had grown bigger.

2. Synthesis of PT AuNRs

The growth medium was prepared as follows: 50 μl of $HAuCl_4$ (50 mM), 17 ml of water, 2.64 ml of CTAC (25 wt.% in water), and 100 μl of CTAB (200 mM) were mixed in a 50 ml plastic vial. 50 μl of ascorbic acid solution (100 mM) were added, and the vial was shaken by hand. 250 μl of aged seeds were then added, and the vial was again shaken by hand. The solution was then kept at room temperature. After 1 h, the solution was centrifuged at 5500 g for 1 h and the supernatant was discarded and replaced by 2 ml of CTAB (2.5 mM). The solution was then centrifuged at 5500 g for 15 min and the supernatant was discarded and replaced by 200 μl of CTAB (1 mM). This protocol yielded PT AuNRs with a LSPR band centered at 750 nm. To obtain AuNRs with a LSPR band centered at 850 nm, the same protocol was followed except that 42 μl of ascorbic acid (100 mM) were added to the growth solution. The PT AuNRs shape yield is estimated to be around 40% in both cases.

3. Purification step of PT AuNRs

PT AuNR batches were also purified by flocculation. 50 μl of AuNR solution were mixed with 70 μl of BDAC (480 mM) in a 2 ml Eppendorf tube. The tubes were then kept at 35°C. After 2 h, the pink supernatant containing nanospheres was removed and replaced by 1 ml of CTAB (10 mM). The solution was centrifuged for 3 min at 12500 g, and the supernatant was removed and replaced by 1 ml of CTAB (2.5 mM). The solution was then centrifuged for 3 min at 12500 g, and the supernatant was removed and replaced by 50 μl of CTAB (1 mM). This concentrated "stock" solution was used for TEM and UV-vis-NIR absorption measurements.

C. Synthesis of AuNR@Ag nanoparticles

Silver-coated AuNRs, hereafter referred to as AuNR@Ag nanoparticles or core-shell NRs, were prepared in two steps according to the protocol published by Tebbe et al.[15] The first step is to synthesize AuNRs to form the core of bimetallic NRs, on which a silver shell is then grown in the second step. Three batches of AuNR@Ag nanoparticles with different amounts of silver were prepared. 50 μl of purified AuNRs in CTAC (1 mM), obtained as described above, were added to 5 ml of CTAC (10 mM) in a 20 ml scintillation vial. 20, 60, and 300 μl of $AgNO_3$ (10 mM) were added and the solutions were slowly stirred in a 60°C oil bath. After 5 min, an equimolar amount (relative to the $AgNO_3$ quantity) of ascorbic acid was added to each solution. The reactions were left under slow stirring for 8 h at 60°C. The vials were loosely capped and were not protected from light. After 8 h, the solutions were transferred to two 2 ml eppendorf tubes and centrifuged three times at 7700 g for 3 min. The supernatant was each time carefully removed and the precipitate was redispersed, in this order, in 1 ml of CTAC (2.5 mM), 1 ml of CTAC (2.5 mM), and finally 50 μl of CTAC (1 mM). These concentrated stock solutions were used for further TEM and UV-vis-NIR absorption measurements. For the larger silver shells (grown with 300 μl of $AgNO_3$), these centrifugation steps produced a yellow supernatant, indicating the presence of silver nanoparticles as a by-product. The supernatant was always discarded, and the centrifugation steps were performed until the maximum absorbance of the supernatant (non-diluted) was less than 0.05. This enabled us to effectively eliminate these undesired by-products, as suggested by their absence in the TEM images.

D. TEM and HRTEM imaging

To estimate experimentally both the nanoparticle length and width and their tip and edge rounding parameters, imaging of the synthesized nanoparticles was performed by using JEOL 1011 and JEOL 2011 microscopes for conventional TEM and HRTEM, respectively. The samples were prepared by depositing 2 μl of colloidal solution onto a copper grid covered by an amorphous carbon film. The length and width distributions were determined using the NIH ImageJ software over a batch of hundreds of particles.

E. HAADF-STEM imaging and STEM-XEDS elemental mapping

High-angle annular dark-field (HAADF) scanning transmission electron microscopy (STEM) yields projection images in which the intensity scales with the thickness of the sample as well as the atomic number Z of the chemical elements of which it consists. HAADF-STEM imaging was performed using a JEOL JEM 2100 Plus microscope operating at an acceleration voltage of 200 kV. X-ray energy dispersive spectra (XEDS) were acquired using the X-Max 80 SDD system from Oxford Instruments. STEM-XEDS element mapping was performed by coupling a x-ray energy dispersive spectrometer to a STEM unit. The STEM-XEDS maps were acquired using the Au Mα and Ag Lα lines.

F. Electrodynamics calculations by the DDA method

Calculations of the extinction spectra were carried out by using the DDA method.[32] This method aims to solve the problem of scattering and absorption by a finite target interacting with a monochromatic plane wave incident from infinity. It is well suited for calculating the absorption coefficients for a wide variety of target geometries.[19,23,33] In DDSCAT, the target is represented by an array of polarizable point dipoles located on a cubic lattice with lattice spacing d. In this work, targets were created to model nanorods or nanocuboids by forming arrays of point dipoles inscribed in superellipsoids whose geometry (length, width, and outline rounding) was designed by ourself to mimic that of the real nano-objects. Multiple plasmon dephasing processes (radiation damping,[34,35] surface-electron scattering,[35–37] and chemical interface damping[38,39]) affect the LSPR of metal nanoparticles with relative contributions that depend on both nanoparticle size and shape. For metallic nanoparticles with dimensions well below the mean free path of the electrons, additional scattering of electrons at the particle surfaces is generally taken into account by introducing a size-dependent Drude contribution to the bulk dielectric function. It should be noted that under the influence of such an additional contribution to the dielectric function, the extinction spectra of AuNRs calculated by DDA generally show a broadening with no shift in the longitudinal LSPR band.[28] For AuNRs larger than 20 nm in width such as those considered in this work, radiation damping is expected to be the dominant effect, while electron-surface scattering should become dominant for those less than 10 nm in width.[35] A numerical approach based on the T-matrix model has already successfully attempted to produce accurate calculations of orientation-averaged extinction spectra from AuNR ensembles, taking into account statistical variations in their shape and size.[40] However, it is also well known that the averaging effect inherent in such ensemble measurements inevitably helps to obscure the intrinsic size effects behind the dielectric function correction mentioned above. For this reason, and because it would be even more difficult to apply the appropriate correction in the case of silver-coated AuNRs, the dielectric functions for gold and silver published by Johnson and Christy[41] were used in all our calculations without any size- or shape-dependent correction term. The lattice spacing d was fixed to 1 nm, and the refractive index of the surrounding medium was set to that of water ($n = 1.33$). The fitting parameters involved in the program to build superellipsoids enabling to model pure AuNRs and AuNR@Ag nanoparticles are quoted, respectively, in Tables S1 and S2 in the supplementary material. Unless otherwise stated, to simulate the random orientation of nanorods and nanocuboids in solution, extinction spectra were calculated by averaging over seven target orientations relative to the polarization of the incident wave.

III. RESULTS AND DISCUSSION

A. Single-crystal and pentatwinned AuNRs

To study the impact of AuNR tip curvature on their optical properties, several batches of AuNRs were prepared with low dispersions in both size and shape. Various synthesis protocols and purification stages by depletion interaction forces were implemented, as described in the Experimental section. Following the protocol described above,[8] SC AuNRs with different aspect ratios but identical tip morphology were synthesized.

Figure 1 represents an example of such samples, while others prepared using the same procedure are shown in Figs. S1-S4 in the supplementary material. Looking at both the representative TEM image and absorption spectrum shown in Fig. 1a,b provides relevant information on the morphology of AuNRs in this first sample. As is typical of AuNRs, the UV-vis-NIR absorption spectrum shows indeed two bands due to LSPR dipolar modes. The band centered around 510 nm arises from the transverse LSPR mode, while the band centered here at 855 nm is related to the longitudinal LSPR mode. In addition to SC AuNR samples, PT AuNRs were synthesized using another protocol.[31] TEM images of these AuNRs and their length, width, and aspect ratio distributions are shown in Figs. S5-S6 in the supplementary material. Hereafter, AuNR samples will be named according to the crystallinity (*SC* for single-crystals and *PT* for pentatwinned AuNRs) and the wavelength λ_{LSPR} measured at the maximum of the longitudinal LSPR band. The full width at half maximum (FWHM) of the longitudinal LSPR band and its profile provide valuable insights into the AuNR size dispersion. As indicated in Table I, the FWHM of the longitudinal LSPR band was measured for each AuNR sample as being of the order of 200 meV, and some even less. These FWHM values are of the same order as those reported on AuNRs reputed to be well calibrated,[8,42] confirming the narrow size distribution of the AuNRs synthesized in this work. In addition, it should be noted that both the absence of any shoulder on the transverse band observed in Fig. 1b and the high value (≈ 6.8) of the absorbance ratio at the maximum of the longitudinal to transverse bands argue in favor of a low overall amount of impurities in sample $SC-855$. This amount should not exceed few percents, in coherence with our observation by TEM of AuNRs from that sample. Numerical analysis of TEM images allows us to accurately assess the NR dimensions. The distributions in AuNR length, width, and aspect ratio determined for sample $SC-855$ are plotted in Fig. 1c-e. The corresponding average AuNR dimensions are estimated to be 90.6 ± 5.2 nm in length, 22.4 ± 1.1 nm in width, and 4.1 ± 0.3 in aspect ratio. The average dimensions determined for all samples of SC and PT AuNRs are quoted in Table I.

To take the analysis of nanorod morphology a step further, we need to associate it with a shape that can be easily modeled. Similar to silver nanocubes studied in a previous work,[26] AuNRs with such small dimensions can be modeled by superellipsoids whose surface is defined by the following implicit equation:

TABLE I. Average length, width, and aspect ratio, as determined from TEM analysis of different samples of SC and PT AuNRs. For each sample, the wavelength λ_{LSPR} and the FWHM of the longitudinal LSPR band are also indicated.

sample name	length (nm)	width (nm)	aspect ratio	λ_{LSPR} (nm)	FWHM (meV)
$SC-667$	57.6 ± 7.3	23.8 ± 2.9	2.4 ± 0.3	667 ± 1	264 ± 6
$SC-756$	96.6 ± 8.0	31.6 ± 2.2	3.1 ± 0.3	756 ± 1	199 ± 5
$SC-816$	99.9 ± 11.3	27.8 ± 1.5	3.6 ± 0.4	816 ± 1	175 ± 4
$SC-855$	90.6 ± 5.2	22.4 ± 1.1	4.1 ± 0.3	855 ± 1	179 ± 4
$SC-882$	87.0 ± 7.3	20.1 ± 0.8	4.3 ± 0.4	882 ± 1	176 ± 4
$PT-753$	68.2 ± 3.5	21.2 ± 0.7	3.2 ± 0.2	753 ± 1	191 ± 5
$PT-857$	79.8 ± 7.0	19.1 ± 1.0	4.2 ± 0.5	857 ± 1	231 ± 4

$$\left|\frac{x}{W/2}\right|^r+\left|\frac{y}{W/2}\right|^r+\left|\frac{z}{L/2}\right|^t=1 \qquad (1)$$

where W is the width of the superellipsoid along the x and y axes and L is the length of its major axis oriented along the z axis (see Fig. S7 in the supplementary material). The exponents r and t are positive real numbers whose values control the rounding of the superellipsoid outlines. The superellipsoid outline along the xy plane is primarily fixed by r and can evolves, in theory, from the circular shape to the perfect square by increasing the r-value from $r=2$ to the limit $r\to\infty$. On its side, the exponent t essentially governs the curvature of the superellipsoid end-cap and will be referred to as the *tip rounding parameter*, below. It is noticeable that the outlines along the xy, yz or zx planes of a superellipsoid whose surface is defined by Eq. 1 are superellipses related to the same r and t values. Such superellipses are ideal outlines to fit the AuNR cross-sections, as seen in a top view as in TEM images. SC AuNRs were demonstrated to show an octogonal cross-section and high-index {520} lateral facets, whereas their PT counterparts display a pentagonal cross-section with {100} lateral facets. However, the small dimensions of the NRs synthesized in this work make these facets poorly pronounced. In practice, one will therefore assume the transverse AuNR cross-section to be circular, meaning that the r-value used to describe it will be fixed to $r_{\mathrm{Au}}=2$ throughout this work. Adjusting L, W, and the tip rounding parameter t makes it possible to satisfactorily model the longitudinal AuNR cross-section. This will be very helpful for simulating the extinction spectra of AuNRs from each sample while properly accounting for their actual morphology.

Interestingly, SC and PT AuNRs do not show identical end-cap geometries due to different tip faceting. This is clearly illustrated in Fig. 2a,b where two representative AuNRs from samples $SC-855$ and $PT-857$ are compared. For these two examples, the more appropriate profile to fit the AuNR cross-section was selected among several superellipses depicted in Fig. 2c for t_{Au} varying from 4 to 16. From a direct comparison of the pictures with the TEM images, it trends out that the profile corresponding to $t_{\mathrm{Au}}=12$ well reproduces the SC AuNR cross-section, whereas that of the PT AuNR is better fitted with the superellipse related to $t_{\mathrm{Au}}=6$.

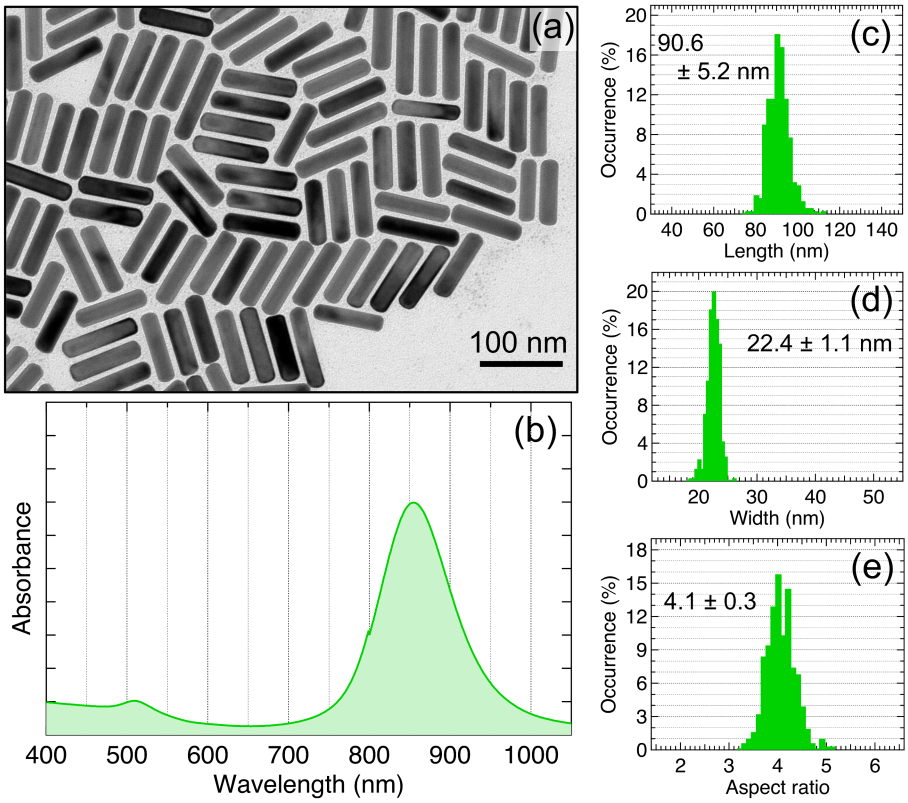

FIG. 1. (a) Representative TEM image and (b) absorption spectrum of SC AuNRs from sample $SC-855$. (c) Length, (d) width and (e) aspect ratio distributions, as determined from TEM images using the imageJ software.

Using superellipsoids for modeling the AuNR morphology, DDA simulations were carried out to analyze successively the impact of the parameters L_{Au}, W_{Au}, and t_{Au} on the extinction spectra. Fig. 3a shows extinction spectra calculated when varying the major axis length L_{Au} at fixed W_{Au} and t_{Au}. Whereas the position of the transverse LSPR band is nearly unchanged around 510 nm, that of the predominant longitudinal band is significantly shifted toward higher wavelengths for increasing L_{Au}. More precisely, the longitudinal band redshifts from 632 to 1024 nm as the superellipsoid aspect ratio increases from around 2 to 5.2. The redshift of the longitudinal band when increasing the AuNR aspect ratio is a well-known result that can be almost similarly obtained by decreasing the superellipsoid width W_{Au} at fixed L_{Au} and t_{Au}, as observed in Fig. 3b. Plotting the wavelength λ_{LSPR} at extinction maximum of the longitudinal band as a function of the superellipsoid aspect ratio (AR) illustrates the existence of a typical plasmon-shape relation (see insets in Fig. 3a,b), expressed as follows:

$$\lambda_{\mathrm{LSPR}} = \alpha \times \mathrm{AR} + \beta, \tag{2}$$

where α and β are real coefficients issued from the linear fit. At this point, the refractive index of the superellipsoid's host medium ($n = 1.33$) and the end-cap shape ($t_{\mathrm{Au}} = 12$) remain unchanged. However, it trends out that the plasmon-shape relationships resulting from the linear fit of these two data sets are not strictly equivalent and depend on how the AuNR aspect ratio is modified. Indeed, the coefficients derived from the first data set are $\alpha = (115.28 \pm 1.55)$ nm and $\beta = (395.89 \pm 6.01)$ nm, whereas those obtained from the second one are $\alpha = (96.97 \pm 1.36)$ nm and $\beta = (470.79 \pm 6.09)$ nm. These plasmon-shape relationships can be compared with those also established for AuNRs from other experimental and theoretical studies.[2,5,6,43]

In both Fig. 3a,b, the calculated spectra of Au superellipsoids are plotted along with the spectrum measured from sample $SC-855$. Logically, this latter spectrum exhibits a more damped profile than the calculated ones due to the various sources of inhomogeneous broadening inherent to ensemble measurement. Nevertheless, there is very good agreement on the position of the LSPR bands between the spectrum measured from this sample and that calculated for a superellipsoid of length $L_{\mathrm{Au}} = 89$ nm and width $W_{\mathrm{Au}} = 22$ nm ($\mathrm{AR} = 4.05$). These L_{Au} and W_{Au} values are very close to the mean length and width of AuNRs from sample $SC-855$, as determined by analysis of TEM images from that sample. Let us now have a look at the evolution of the measured λ_{LSPR} as a function of the aspect ratio, as estimated from all of the other SC AuNR samples (Fig. S8 in the supplementary material). One found out a similar plasmon-shape relationship as that derived from our DDA calculations [Eq. 2] with the following linear fit coefficients: $\alpha = (110.97 \pm 5.4)$ nm and $\beta = (406.82 \pm 19.3)$ nm. This consistency between the AuNR dimensions provided by TEM analysis and our DDA calcula-

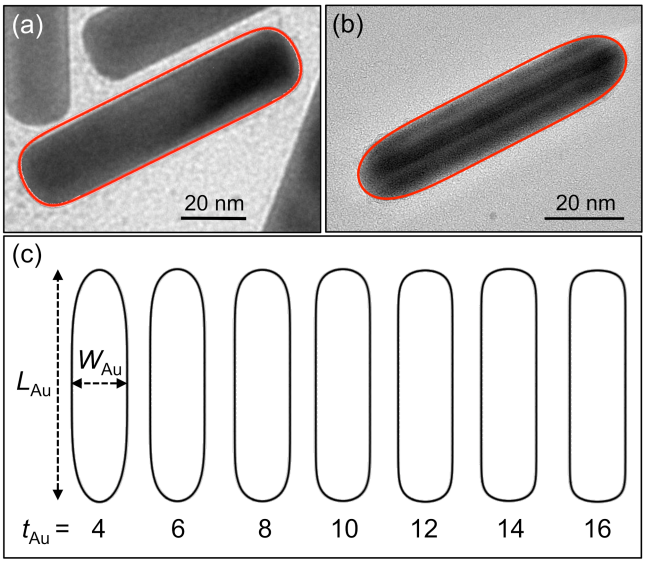

FIG. 2. Modeling the end-cap geometry of AuNRs by superellipse profiles. TEM images of (a) one representative SC AuNR from sample $SC-855$. The cross-section of this NR is outlined with a superellipse profile (in red color) corresponding to $t_{Au}=12$. (b) TEM image of one representative PT AuNR from sample $PT-857$. Its cross-section is well fitted using a superellipse profile defined by $t_{Au}=6$. (c) Superellipse profiles used for modeling the cross-section of nanorods. Each profile is defined by the length L_{Au} of the major axis, its width W_{Au}, and the tip rounding parameter t_{Au} related to the end-cap curvature. The profiles depicted correspond to t_{Au} ranging from 4 to 16.

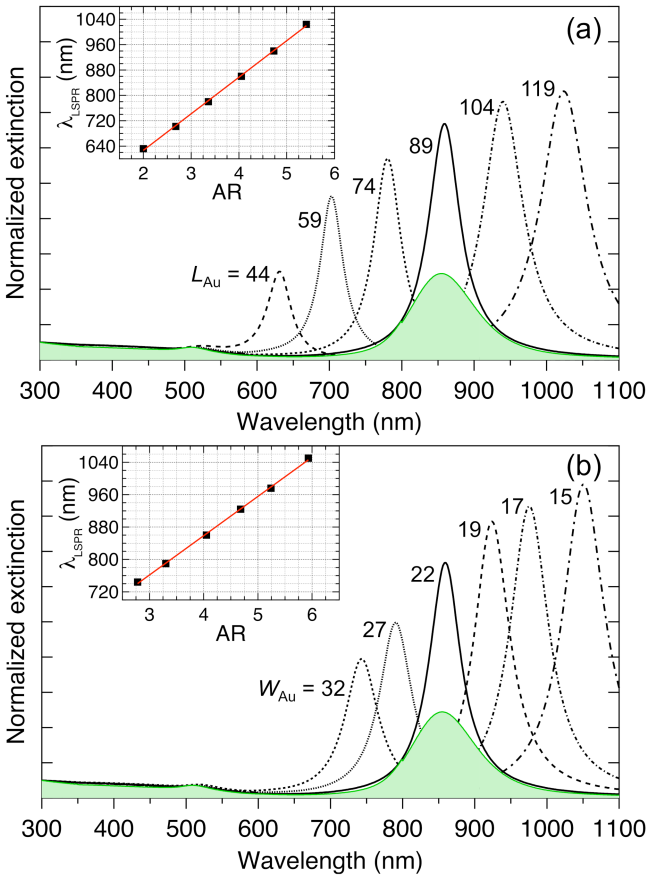

FIG. 3. Extinction spectra of Au superellipsoids calculated using the DDA method. (a) DDA spectra of AuNRs simulated as superellipsoids of different major axis lengths ($44 \le L_{Au} \le 119$ nm), at fixed width ($W_{Au}=22$ nm). (b) DDA spectra of AuNRs simulated as superellipsoids of different widths ($15 \le W_{Au} \le 32$ nm), at fixed length ($L_{Au}=89$ nm). In both panels, the DDA spectra are plotted along with that measured from sample $SC-855$ (green shaded spectrum). The insets in (a) and (b) show the evolution of the wavelength at extinction maximum λ_{LSPR} as a function of aspect ratio (AR). The red line is the linear fit of the data. For all calculations, the tip rounding parameter was fixed to $t_{Au}=12$ and spectra were normalized with respect to the extinction at 300 nm.

tions supports the modeling of these nano-objects by superellipsoids within the DDA method. It also validates our strategy of using this approach to examine the impact of the tip morphology of AuNRs on their optical response.

Figure 4 shows the evolution of the superellipsoid's extinction spectrum when the tip rounding parameter t_{Au} is varied while keeping its length and width constant ($L_{Au}=89$ nm and $W_{Au}=22$ nm). By changing the morphology of the target from a cylinder with rounded edges ($t_{Au}=16$) to a cigar-shaped superellipsoid ($t_{Au}=4$), the longitudinal LSPR band is clearly blueshifted. As shown in the inset, this blueshift corresponds to the decrease in λ_{LSPR} from 868 to 822 nm. The shift in the longitudinal band is all the more pronounced at lower values of the tip rounding parameter, i.e., when the evolution of the superellipsoid's morphology is most significant. Here again, a comparison of the calculated spectra with that measured from the sample $SC-855$ confirms our TEM observations in that the best agreement is obtained for t_{Au} between 10 and 12 [Fig. 2a].

On this basis, it is interesting to compare the wavelengths λ_{LSPR} measured from SC and PT AuNRs with nearly identical aspect ratios but different tip curvatures (see Table I and Fig. 2). The average AuNR aspect ratio estimated from sample $SC-855$ is very slightly lower than that of AuNRs from sample $PT-857$. The same applies to AuNRs from samples $SC-756$ and $PT-753$. Taking into account only the dependence of λ_{LSPR} on the aspect ratio, as described by Eq. 2, a redshift of the longitudinal band of around 10 nm would be expected from SC to PT AuNRs, in both examples. However, the increase in λ_{LSPR} reaches only 2 nm from sample $SC-855$ to $PT-857$, whereas a slight blueshift of the longitudinal LSPR band is even observed for $PT-753$ compared to $SC-756$. Such a trend is likely to originate from the variation of the AuNR tip curvature. As a matter of fact, the slight increase in the aspect ratio, on the one hand, and the more rounded tip in PT AuNRs, on the other hand, have antagonistic effects on the position of the LSPR band whose potential shift is therefore difficult to predict in that case. It is, nevertheless, striking to note that a seemingly small change in morphology can lead to perceptible shifts in the longitudinal band, even for ensemble measurements, such as those we are dealing with in this study. Furthermore, the reliability of the

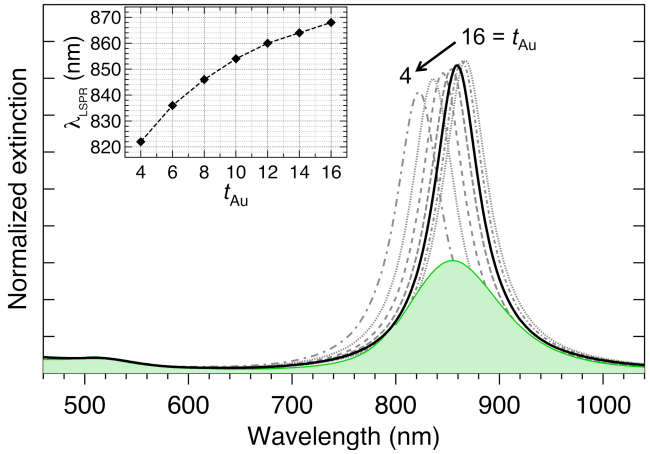

FIG. 4. DDA spectra of Au superellipsoids of various end-cap geometries associated with a tip rounding parameter t_{Au} ranging from 4 to 16, at fixed length ($L_{Au} = 89$ nm) and width ($W_{Au} = 22$ nm). These calculated spectra are plotted along with that measured from sample $SC-855$ (green shaded spectrum). The black continuous line corresponds to the spectrum calculated for $t_{Au} = 12$. All spectra were normalized with respect to the extinction at 300 nm. The inset shows the evolution of the wavelength at extinction maximum λ_{LSPR} as a function of t_{Au}.

DDA method applied to superellipsoid-shaped targets to simulate the extinction spectra of AuNRs shows the relevance of using this approach to analyze the spectra measured from such nano-objects. Exploiting the same approach, this study is extended below to the case a bit more complex of bimetallic (Au core)–(Ag shell) nanoparticles.

B. Silver-coated AuNRs

Low AuNR size and shape distributions are required to promote the synthesis of well-calibrated AuNR@Ag nanoparticles. The single-component AuNR samples presented in Subsection III A offered several possible choices meeting these criteria (see Table I). Among them, AuNRs from sample $SC-855$ were chosen to serve as core materials for the synthesis of all the AuNR@Ag nanoparticles we will be studying next. As mentioned earlier, three batches of AuNR@Ag nanoparticles were prepared by adjusting the amount of silver nitrate, thereby modifying both the thickness and morphology of the silver shell. From previous studies, it is already known that silver growth is anisotropic. As shown in the TEM image of AuNR@Ag nanoparticles presented in Fig. 5, the silver shell thickness is not the same in the transverse and longitudinal directions.[10,15] In addition, from that sample, the silver shell clearly exhibits rectangular outlines with rounded corners. It is worth noting that such a rectangular outline agrees with the final cuboidal morphology that is expected for the AuNR@Ag nanoparticles synthesized here. Indeed, with regard to the silver shell growth mechanism in aqueous solution, it has been shown that adsorption of chloride counterions on the presynthesized AuNRs helps to stabilize {100} facets by

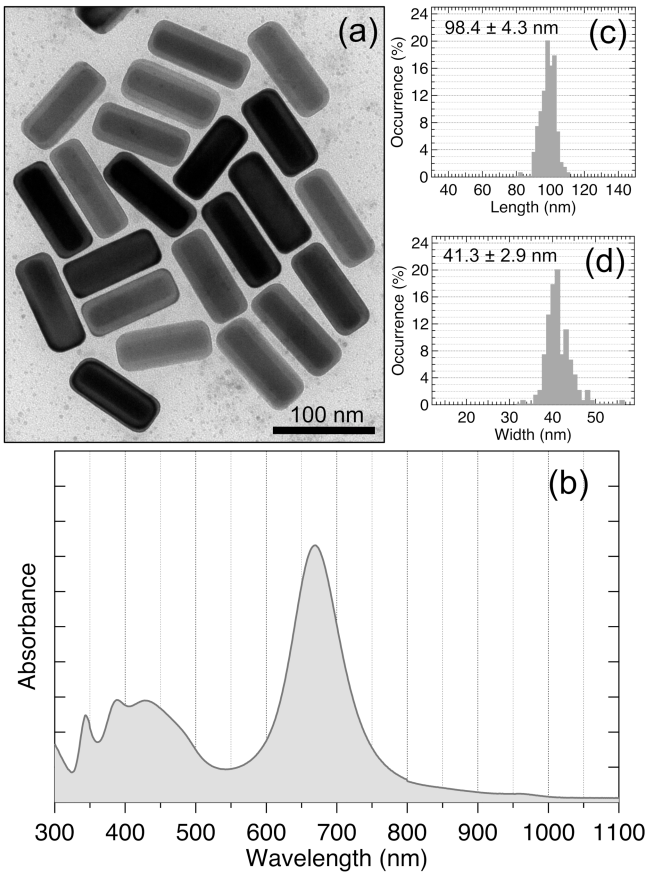

FIG. 5. (a) Representative TEM image and (b) absorption spectrum of core-shell NRs from sample *AuNR@Ag*(670). (c) Length and (d) width distributions, as determined from TEM images of those core-shell NRs.

significantly reducing their surface free energy compared to other crystallographic facets. For a high enough $[Ag^+]/[Au^0]$ molar ratio, the silver shell growth is thus likely to lead to the formation of well-defined AuNR@Ag cuboids enclosed by six {100} facets.[44] Three batches of AuNR@Ag nanoparticles were prepared using different amounts of $AgNO_3$ to grow silver shells of different thicknesses and morphologies from batch to batch.

Figures 5, S9, and S10 in the supplementary material each shows a representative TEM image, the length, and width distributions from these three AuNR@Ag nanoparticle batches and their absorbance spectra. Thanks to a slight variation in contrast between the two metals, it is easy to see from the TEM images that there is a clear difference in silver shell thickness from one sample to the next. As expected, it is also clear that the morphology of the silver shell evolves with its thickness. For the sample with the lowest Ag^+ concentration, the overall shape of AuNR@Ag nanoparticles remains roughly conformal to that of the core AuNRs (Fig. S9a). In contrast, the silver shell adopts a cuboidal morphology for the other two samples, with the edge sharpness increasing with Ag^+ concentrations [see Fig. 5a and Fig. S10a in the supplementary material], which is perfectly in line with work already

TABLE II. Average length, width, and aspect ratio, as determined from TEM analysis of different AuNR@Ag nanoparticle samples. For each sample, the wavelength λ_{LSPR} of the longitudinal LSPR is indicated.

sample name	length (nm)	width (nm)	aspect ratio	λ_{LSPR} (nm)
AuNR@Ag(767)	93.5 ± 5.6	28.5 ± 2.2	3.3 ± 0.3	767 ± 1
AuNR@Ag(670)	98.4 ± 4.3	41.3 ± 2.9	2.4 ± 0.2	670 ± 1
AuNR@Ag(619)	108.8 ± 4.8	63.3 ± 2.6	1.7 ± 0.1	619 ± 1

published elsewhere.[15] The TEM image of the largest cuboids in Fig. S10a shows that several AuNR@Ag nanoparticles can easily stand up on the large square {100} facets at their ends. This allows us to observe these cuboids from two distinct directions, perpendicular and parallel to their long axis, and thus verify that the core AuNRs are indeed at the center. Mass-thickness contrast images recorded using HAADF-STEM and STEM-XEDS elemental maps show clearly the positioning of the core AuNR in the center of the silver shell, as illustrated for the largest cuboids in the supplementary material (see Fig. S11).

The simultaneous evolution of the morphology and composition of AuNR@Ag nanoparticles, resulting from variations in the [Ag]/[Au] molar ratio, is accompanied by significant changes in their absorbance spectrum. The first change to note is the blueshift of the longitudinal LSPR band. Whereas this band was centered at 855 nm with single-component AuNRs from sample $SC-855$, it shifts successively to 767, 670, and then 619 nm for AuNR@Ag nanoparticles coated with an increasingly thick silver shell. As with AuNRs, this remarkable feature will be used below to name the various AuNR@Ag nanoparticle samples whose corresponding dimensions are quoted in Table II. This blueshift of the longitudinal band originates from the combined effects of the reduced aspect ratio and the increased contribution of silver to the optical response of the nanoparticles.[13,15,45] In other words, the more advanced the overgrowth process, i.e., the thicker the silver shell, the more the LSPR modes of the silver cuboid dominate over those of the AuNR. Except for the blueshift of the longitudinal band, the profile of the absorbance spectrum recorded from sample *AuNR@Ag*(767), which is plotted in Fig. S9b, is quite similar to that of sample $SC-855$. Both spectra remain dominated by the bands corresponding to the longitudinal and transverse dipolar LSPR modes. Note that the transverse LSPR band also undergoes a blueshift, but to a much lesser extent than its longitudinal counterpart, with its maximum shifting from 509 to 498 nm. As the amount of Ag precursor is increased and the silver coating thickens, the transversal band appears to further blueshift, while also intensifying. In sample *AuNR@Ag*(619), this band is centered at 448 nm and is more intense than that of the longitudinal LSPR mode. In addition, new LSPR bands emerge below 500 nm, their number, positions, and profiles depending on the core-shell cuboid morphology [Figs. 5b and S10b]. Here again, the ability to observe and resolve these LSPR modes through ensemble measurements is a reliable indication of the low size and shape distributions that characterize the core-shell NR samples. The additional modes observed at shorter wavelengths than the longitudinal and transverse dipolar modes are likely to be octupolar ones.[45] The corresponding band maxima are positioned at 344 and 390 nm for sample *AuNR@Ag*(670) and at 348 and 393 nm for sample *AuNR@Ag*(619). These two bands therefore show a barely perceptible redshift as the silver shell thickens and its outer shape become cuboidal.

Independently controlling the shell's dimensions (length and width) and its morphology, through the rounding of its edges, is a very complicated task with core-shell cuboids. In this respect, numerical simulation using the DDA method provides an easy and effective way for overcoming this limitation. As we first illustrated by studying single-component AuNRs with different end shapes, it is worth investigating how of morphological features such as rounded shell edges can influence the optical response of core-shell cuboids. This is all the more relevant as TEM allows us to assess this shape parameter, but only on the scale of a few nanoparticles considered to be representative of the batch from which they come from. One of the advantages of simulating AuNRs with a superellipsoid target is that this approach can also be applied to core-shell cuboids. Here again, the first step is to design a target based on an array of point dipoles whose outer boundaries follow the shape of the silver shell as closely as possible. Depending on their location within the lattice, the dipoles are assigned the polarizability of either silver or gold. The dielectric function of gold was therefore attributed to all point dipoles located in the volume of the superellipsoid that best represented AuNRs from sample $SC-855$. For all the subsequent core-shell cuboid target, the fitting parameters defining the core AuNR were systematically set to the following values: $L_{\mathrm{Au}} = 89$ nm, $W_{\mathrm{Au}} = 22$ nm, $r_{\mathrm{Au}} = 2$ and $t_{\mathrm{Au}} = 12$. TEM images are used to make an initial estimate of the tip and rounding parameters of the silver shell, which will be noted as t_{Ag} and r_{Ag}, respectively. As an example, Fig. S12 compares the typical profile of core-shell cuboids from sample *AuNR@Ag*(670), as imaged by TEM, to those of different superellipses, providing $t_{\mathrm{Ag}} = 10$ and $r_{\mathrm{Ag}} = 4$ as optimum parameters to simulate cuboids from that sample. For each sample, the fitting parameters L_{Ag} and W_{Ag} used to scale the modeled silver shell were roughly set to the measured dimensions. All the fitting parameters used for calculating the extinction spectra of AuNR@Ag superellipsoids are quoted in Table S2 in the supplementary material. Some of the DDA targets designed to model each of the three AuNR@Ag nanoparticle types are shown schematically in Figs. S13-S15.

Unlike the AuNRs, whose edge-rounding parameter was fixed at $r_{\mathrm{Au}} = 2$ and only the end-rounding parameter t_{Au} was variable, the silver shell profile of AuNR@Ag nanoparticles changes from sample to sample, in both transverse and longitudinal cross-sections. This profile is defined by the rounding parameters r_{Ag} and t_{Ag}, the values of which will be refined by DDA simulations. To this end, the extinction spectra of AuNR@Ag superellipsoids were calculated by giving these two parameters realistic values, i.e., close to those obtained from TEM images with each batch of nanoparticles.

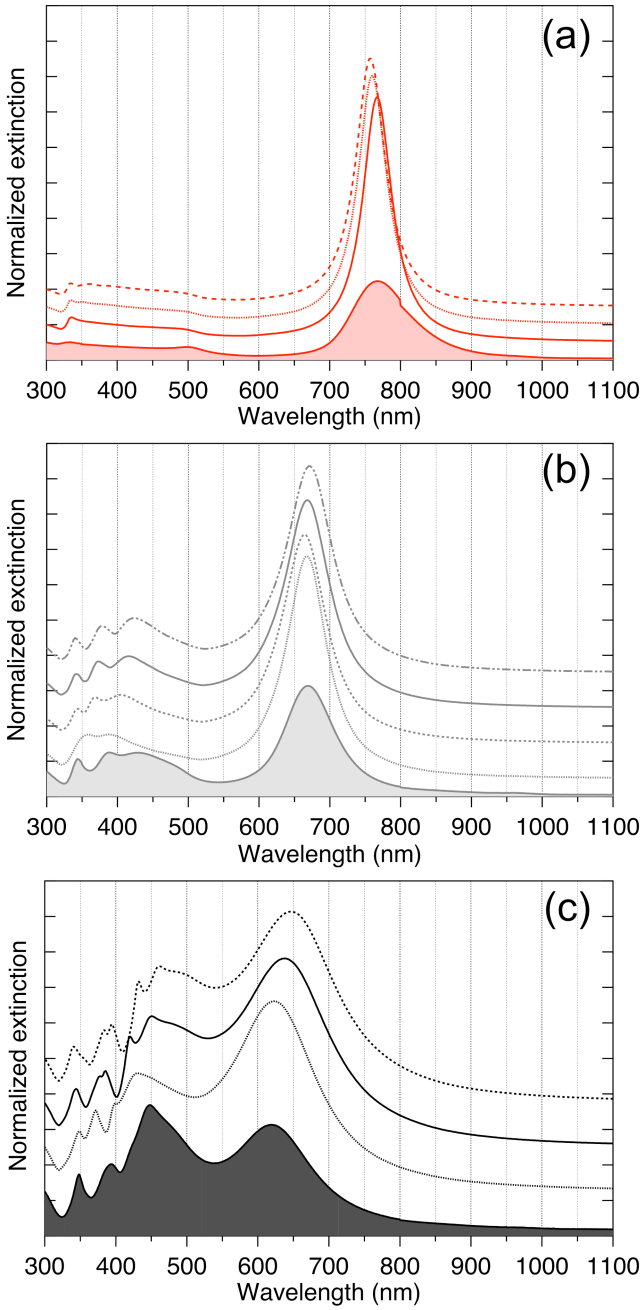

FIG. 6. Dependence of the extinction spectra of AuNR@Ag superellipsoids on the silver shell morphology, as modeled by varying the edge rounding parameter r_{Ag} while fixing the tip rounding parameter to $t_{Ag} = 10$. (a) Comparison of the spectrum measured from sample *AuNR@Ag*(767) (red shaded curve) with those calculated by using $L_{Ag} = 93$ nm, $W_{Ag} = 28$ nm, and $r_{Ag} = 2$, 2.5, and 3, from bottom to top. (b) Comparison of the spectrum measured from sample *AuNR@Ag*(670) (gray shaded curve) with those calculated by using $L_{Ag} = 98$ nm, $W_{Ag} = 41$ nm, and $r_{Ag} = 2$, 3, 4, and 5, from bottom to top. (c) Comparison of the spectrum measured from sample *AuNR@Ag*(619) (black shaded curve) with those calculated by using $L_{Ag} = 107$ nm, $W_{Ag} = 63$ nm, and $r_{Ag} = 3$, 6, and 9, from bottom to top. All spectra were normalized with respect to the extinction at 300 nm and vertically shifted for clarity.

Figure S16, in the supplementary material, illustrates for each sample the weak dependence of the extinction spectrum on the parameter t_{Ag}. By using plausible parameters for carrying out the calculations, it appears that the DDA spectra are in good agreement with those measured from each batch of core-shell NRs. Increasing t_{Ag} from 8 to 12 leads only to a very slight redshift of the longitudinal LSPR mode band and has virtually no impact on the profile of the multiple LSPR bands. Even though the redshift is small in all cases, it is, nonetheless, noticeable that as the silver shell becomes thinner, the redshift increases. This can easily be understood in the sense that the thinner the silver shell at the ends of the superellipsoid, the more sensitive to any change in the shell thickness the core AuNR longitudinal LSPR mode should be. To a certain extent, we conclude that the choice of the tip rounding parameter is not so as critical for cuboids as it was for AuNRs, and for the sake of simplification, we have chosen to keep $t_{Ag} = 10$ to study the dependence of the extinction spectra on the edge rounding parameter r_{Ag}. This is illustrated in Fig. 6 where we compare spectra measured from each sample with those calculated for several values of r_{Ag}. By varying r_{Ag} around a representative value, as derived from the TEM images, it emerges that the superellipsoids with the thickest silver shells are more sensitive to variations in the edge rounding. Indeed, when r_{Ag} increases slightly, the amount of silver covering the core AuNR also increases and, for the superellipsoid with the thinnest silver shell, only a slight blueshift of the longitudinal band is observed in Fig. 6a. Conversely, for superellipsoids with thicker silver shells, the variation in r_{Ag} is manifested by a change in allure as well as a shift of certain bands of the octupolar LSPR modes [Fig. 6b,c].

The impact of edge rounding is much more pronounced when a very large variation is applied to the r_{Ag} parameter. To illustrate this, the extinction spectrum calculated for a superellipsoid whose shell has extremely sharp edges is plotted in Fig. S17 in the supplementary material. For such sharp edges, we observe an increase in the number of LSPR bands below 500 nm, most of which have an apparent substructure. The analysis of all the bands observed is very complex, and the complete attribution of these different bands would require an entire study, which is beyond the scope of this work. Nevertheless, it is possible to take our analysis a step further by calculating the extinction spectra of a superellipsoid whose major axis is either parallel or perpendicular to the polarization of the incident wave. The spectra calculated in these two configurations for the superellipsoid with the thickest silver shell are shown in Fig. S18. From these spectra, it is easy to identify the transverse and longitudinal components of the observed LSPR modes and to gain a better understanding of the appearance of certain bands whose substructure can thus be decomposed. This is particularly true for the band attributed to the transverse dipolar LSPR mode on the spectrum of the *AuNR@Ag*(619) sample [see either Fig. 6c or Fig. S10 in the supplementary material], which turns out to be the envelope of both transverse and longitudinal modes. Taking the rounding of cuboid edges into account as carefully as possible can therefore be of real benefit when reading and interpreting their extinction spectra. Conversely, provided that a population of

NRs or cuboids have sufficiently low dispersions of size and shape, their extinction spectra are likely to provide quantitative information on morphological features, such as the rounding of their tips or edges.

IV. CONCLUSIONS

AuNRs and Au@Ag core-shell cuboids of various sizes and morphological characteristics were prepared using seeded growth synthesis protocols. These synthesis processes yielded several populations of nano-objects with small size and shape distributions. Absorption spectroscopy measurements carried out on these populations of well-calibrated nano-objects enabled us to observe changes in their optical response resulting from subtle variations in morphology. The profile of the spectra changes mainly in the most intense band corresponding to the longitudinal LSPR mode. Experimentally, it is clear that this LSPR band redshifts significantly as the aspect ratio of the nanorods increases. However, by comparing the spectra of SC AuNRs with those recorded from polycrystalline ones, with more rounded cap-ends, we note that such a slight change in shape is not trivial since it contributes to modifying the relationship between the position of the longitudinal LSPR band and the AuNR aspect ratio. Furthermore, in the case of Au@Ag core-shell cuboids, the growth of the silver shell covering the core AuNR was accompanied by a very significant change in its shape, becoming cubic with increasingly sharp edges. This change in morphology led to the emergence of additional plasmon modes, octupolar in nature and attributable both to the evolution of the shell morphology and to the increasing contribution of silver to the overall optical response of the cuboid. Numerical simulations based on the DDA method, assimilating AuNRs or core-shell Au@Ag cuboids to superellipsoids, were carried out to support the interpretation of the measured spectra. Although based on the extinction of a single particle, the profile of the calculated spectra shows good agreement with that of our ensemble measurements, validating the approach adopted for these calculations. As with the AuNRs, the DDA calculations show just how important it is to take proper account of the rounding of the silver shell edges when modeling the cuboid shape. Modeling a cuboid with excessively rounded or sharp edges leads to the disappearance or, on the contrary, the emergence of LSPR bands in the extinction spectrum and would not allow experimental data to be adequately reproduced. Conversely, provided that the average dimensions of a population of well-calibrated nanorods are known, a fairly accurate assessment of the average shape of their end-caps is possible by analyzing their optical response. This further extends the already recognized ability of absorption spectroscopy to characterize a population of nanorods as a complement to TEM analysis and can therefore be useful for all applications where the precise morphology of these nano-objects matters.

SUPPLEMENTARY MATERIAL

See the supplementary material for characterization data (absorbance spectra, TEM images, and length, width, and aspect ratio distributions) collected for various batches of colloidal AuNRs and AuNR@Ag nanoparticles (supplemental figures) and fitting parameters used to carry out the DDA calculations, schematics of DDA targets, and some additional extinction spectra calculated by the DDA method (supplemental tables).

ACKNOWLEDGMENTS

The authors thank Dr. N. Goubet from Sorbonne Université (MONARIS, UMR 8233 CNRS-SU) for imaging AuNRs and Au@Ag core-shell cuboids by HRTEM and performing HAADF-STEM EDX measurements. The authors also thank Dr. B. Madebène, from the same laboratory, for his advice on running the DDSCAT program using the computing resources of the Jarvis platform (IP_2CT, FR2622).

AUTHOR DECLARATIONS

Conflict of interest

The authors have no conflicts to disclose.

Author contributions

Charles Vernier: Conceptualization (equal); Investigation (lead); Formal analysis (equal); Writing - original draft (supporting); Writing - review and editing (supporting).

Hervé Portalès: Conceptualization (equal); Supervision (lead); Formal analysis (equal); Writing - original draft (lead); Writing - review and editing (lead).

DATA AVAILABILITY STATEMENT

The data that support the findings of this study are available within the article and its supplementary material. The DDA method used to calculate the extinction spectra was applied using the DDSCAT 7.3 freely available open-source software package (https://www.astro.princeton.edu/~draine/DDSCAT.7.3.html).

REFERENCES

[1]J. Pérez-Juste, I. Pastoriza-Santos, L. M. Liz-Marzán, and P. Mulvaney, "Gold nanorods: Synthesis, characterization and applications," Coord. Chem. Rev. **249**, 1870–1901 (2005).

[2]X. Huang, S. Neretina, and M. A. El-Sayed, "Gold nanorods: From synthesis and properties to biological and biomedical applications," Adv. Mater. **21**, 4880–4910 (2009).

[3]H. Chen, L. Shao, Q. Li, and J. Wang, "Gold nanorods and their plasmonic properties," Chem. Soc. Rev. **42**, 2679–2724 (2013).
[4]J. Zhou, Z. Cao, N. Panwar, R. Hu, X. Wang, J. Qu, S. C. Tjin, G. Xu, and K.-T. Yong, "Functionalized gold nanorods for nanomedicine: Past, present and future," Coord. Chem. Rev. **352**, 15–66 (2017).
[5]S. Link, M. B. Mohamed, and M. A. El-Sayed, "Simulation of the optical absorption spectra of gold nanorods as a function of their aspect ratio and the effect of the medium dielectric constant," J. Phys. Chem. B **103**, 3073–3077 (1999).
[6]S. Link and M. A. El-Sayed, "Simulation of the optical absorption spectra of gold nanorods as a function of their aspect ratio and the effect of the medium dielectric constant," J. Phys. Chem. B **109**, 10531–10532 (2005).
[7]M. Grzelczak, A. Sánchez-Iglesias, B. Rodríguez-González, R. Alvarez-Puebla, J. Pérez-Juste, and L. M. Liz-Marzán, "Influence of iodide ions on the growth of gold nanorods: Tuning tip curvature and surface plasmon resonance," Adv. Funct. Mater. **18**, 3780–3786 (2008).
[8]X. Ye, C. Zheng, J. Chen, Y. Gao, and C. B. Murray, "Using binary surfactant mixtures to simultaneously improve the dimensional tunability and monodispersity in the seeded growth of gold nanorods," Nano Lett. **13**, 765–771 (2013).
[9]L. Scarabelli, A. Sánchez-Iglesias, J. Pérez-Juste, and L. M. Liz-Marzán, "A "tips and tricks" practical guide to the synthesis of gold nanorods," J. Phys. Chem. Lett. **6**, 4270–4279 (2015).
[10]Y. Okuno, K. Nishioka, A. Kiya, N. Nakashima, A. Ishibashi, and Y. Niidome, "Uniform and controllable preparation of au-ag core-shell nanorods using anisotropic silver shell formation on gold nanorods," Nanoscale **2**, 1489–1493 (2010).
[11]J. Becker, I. Zins, A. Jakab, Y. Khalavka, O. Schubert, and C. Sönnichsen, "Plasmonic focusing reduces ensemble linewidth of silver-coated gold nanorods," Nano Lett. **8**, 1719–1723 (2008).
[12]M. Fernanda Cardinal, B. Rodríguez-González, R. A. Alvarez-Puebla, J. Pérez-Juste, and L. M. Liz-Marzán, "Modulation of localized surface plasmons and sers response in gold dumbbells through silver coating," J. Phys. Chem. C **114**, 10417–10423 (2010).
[13]X. Dong, J. Zhou, X. Liu, D. Lin, and L. Zha, "Preparation of monodisperse bimetallic nanorods with gold nanorod core and silver shell and their plasmonic property and sers efficiency," J. Raman Spectrosc. **45**, 431–437 (2014).
[14]J. E. S. van der Hoeven, T.-S. Deng, W. Albrecht, L. A. Olthof, M. A. van Huis, P. E. de Jongh, and A. van Blaaderen, "Structural control over bimetallic core-shell nanorods for surface-enhanced raman spectroscopy," ACS Omega **6**, 7034–7046 (2021).
[15]M. Tebbe, C. Kuttner, M. Mayer, M. Maennel, N. Pazos-Perez, T. A. König, and A. Fery, "Silver-overgrowth-induced changes in intrinsic optical properties of gold nanorods: From noninvasive monitoring of growth kinetics to tailoring internal mirror charges," J. Phys. Chem. C **119**, 9513–9523 (2015).
[16]B. N. Khlebtsov, Z. Liu, J. Ye, and N. G. Khlebtsov, "Au@ag core/shell cuboids and dumbbells: Optical properties and sers response," J. Quant. Spectrosc. Radiat. Transfer **167**, 64–75 (2015).
[17]B. Khlebtsov, V. Khanadeev, and N. Khlebtsov, "Surface-enhanced raman scattering inside au@ag core/shell nanorods," Nano Research **9**, 2303–2318 (2016).
[18]A.-I. Henry, J. M. Bingham, E. Ringe, L. D. Marks, G. C. Schatz, and R. P. Van Duyne, "Correlated structure and optical property studies of plasmonic nanoparticles," J. Phys. Chem. C **115**, 9291–9305 (2011).
[19]C. Noguez, "Surface plasmons on metal nanoparticles: The influence of shape and physical environment," J. Phys. Chem. C **111**, 3806–3819 (2007).
[20]V. Myroshnychenko, J. Rodrìguez-Fernàndez, I. Pastoriza-Santos, A. M. Funston, C. Novo, P. Mulvaney, L. M. Liz-Marzàn, and F. J. Garcìa de Abajo, "Modelling the optical response of gold nanoparticles," Chem. Soc. Rev. **37**, 1792–1805 (2008).
[21]J. Zhao, A. O. Pinchuk, J. M. McMahon, S. Li, L. K. Ausman, A. L. Atkinson, and G. C. Schatz, "Methods for describing the electromagnetic properties of silver and gold nanoparticles," Acc. Chem. Res. **41**, 1710–1720 (2008).
[22]P. Yang, H. Portalès, and M.-P. Pileni, "Identification of multipolar surface plasmon resonances in triangular silver nanoprisms with very high aspect ratios using the DDA method," J. Phys. Chem. C **113**, 11597–11604 (2009).
[23]P. Yang, H. Portalès, and M.-P. Pileni, "Dependence of the localized surface plasmon resonance of noble metal quasispherical nanoparticles on their crystallinity-related morphologies," J. Chem. Phys. **134**, 024507 (2011).
[24]P. Yang, H. Portalès, and M.-P. Pileni, "Ability to discern the splitting between longitudinal and transverse plasmon resonances in Au compared to Ag nanoparticles in close-packed planar arrays," Phys. Rev. B **81**, 205405 (2010).
[25]S. Lee, H. Portalès, M. Walls, P. Beaunier, N. Goubet, B. Tremblay, J. Margueritat, L. Saviot, and A. Courty, "Versatile and robust synthesis process for the fine control of the chemical composition and core-crystallinity of spherical core-shell Au@Ag nanoparticles," Nanotechnology **32**, 095604 (2020).
[26]C. Vernier, L. Saviot, Y. Fan, A. Courty, and H. Portalès, "Sensitivity of localized surface plasmon resonance and acoustic vibrations to edge rounding in silver nanocubes," ACS Nano **17**, 20462–20472 (2023).
[27]K.-S. Lee and M. A. El-Sayed, "Dependence of the enhanced optical scattering efficiency relative to that of absorption for gold metal nanorods on aspect ratio, size, end-cap shape, and medium refractive index," J. Phys. Chem. B **109**, 20331–20338 (2005).
[28]E. S. Kooij and B. Poelsema, "Shape and size effects in the optical properties of metallic nanorods," Phys. Chem. Chem. Phys. **8**, 3349–3357 (2006).
[29]S. W. Prescott and P. Mulvaney, "Gold nanorod extinction spectra," J. Appl. Phys. **99**, 123504 (2006).
[30]K. Park, H. Koerner, and R. A. Vaia, "Depletion-induced shape and size selection of gold nanoparticles," Nano Lett. **10**, 1433–1439 (2010).
[31]A. Sánchez-Iglesias, K. Jenkinson, S. Bals, and L. M. Liz-Marzán, "Kinetic regulation of the synthesis of pentatwinned gold nanorods below room temperature," J. Phys. Chem. C **125**, 23937–23944 (2021).
[32]B. T. Draine and P. J. Flatau, "Discrete-dipole approximation for scattering calculations," J. Opt. Soc. Am. A **11**, 1491–1499 (1994).
[33]B. J. Wiley, S. H. Im, Z.-Y. Li, J. McLellan, A. Siekkinen, and Y. Xia, "Maneuvering the surface plasmon resonance of silver nanostructures through shape-controlled synthesis," J. Phys. Chem. B **110**, 15666–15675 (2006).
[34]C. Sönnichsen, T. Franzl, T. Wilk, G. von Plessen, J. Feldmann, O. Wilson, and P. Mulvaney, "Drastic reduction of plasmon damping in gold nanorods," Phys. Rev. Lett. **88**, 077402 (2002).
[35]C. Novo, D. Gomez, J. Perez-Juste, Z. Zhang, H. Petrova, M. Reismann, P. Mulvaney, and G. V. Hartland, "Contributions from radiation damping and surface scattering to the linewidth of the longitudinal plasmon band of gold nanorods: A single particle study," Phys. Chem. Chem. Phys. **8**, 3540–3546 (2006).
[36]U. Kreibig and L. Genzel, "Optical absorption of small metallic particles," Surf. Sci. **156**, 678–700 (1985).
[37]M. Hu, C. Novo, A. Funston, H. Wang, H. Staleva, S. Zou, P. Mulvaney, Y. Xia, and G. V. Hartland, "Dark-field microscopy studies of single metal nanoparticles: Understanding the factors that influence the linewidth of the localized surface plasmon resonance," J. Mater. Chem. **18**, 1949–1960 (2008).
[38]B. Foerster, A. Joplin, K. Kaefer, S. Celiksoy, S. Link, and C. Sönnichsen, "Chemical interface damping depends on electrons reaching the surface," ACS Nano **11**, 2886–2893 (2017).
[39]B. Foerster, V. A. Spata, E. A. Carter, C. Sönnichsen, and S. Link, "Plasmon damping depends on the chemical nature of the nanoparticle interface," Sci. Adv. **5**, eaav0704 (2019).
[40]B. Khlebtsov, V. Khanadeev, T. Pylaev, and N. Khlebtsov, "A new t-matrix solvable model for nanorods: Tem-based ensemble simulations supported by experiments," J. Phys. Chem. C **115**, 6317–6323 (2011).
[41]P. B. Johnson and R. W. Christy, "Optical constants of the noble metals," Phys. Rev. B **6**, 4370–4379 (1972).
[42]G. González-Rubio, V. Kumar, P. Llombart, P. Díaz-Núñez, E. Bladt, T. Altantzis, S. Bals, O. Peña Rodríguez, E. G. Noya, L. G. MacDowell, A. Guerrero-Martínez, and L. M. Liz-Marzán, "Disconnecting symmetry breaking from seeded growth for the reproducible synthesis of high quality gold nanorods," ACS Nano **13**, 4424–4435 (2019).
[43]A. Brioude, X. C. Jiang, and M. P. Pileni, "Optical properties of gold nanorods: DDA simulations supported by experiments," J. Phys. Chem. B **109**, 13138–13142 (2005).
[44]S. Gómez-Graña, B. Goris, T. Altantzis, C. Fernández-López, E. Carbó-Argibay, A. Guerrero-Martínez, N. Almora-Barrios, N. López, I. Pastoriza-Santos, J. Pérez-Juste, S. Bals, G. Van Tendeloo, and L. M. Liz-Marzán, "Au@Ag nanoparticles: Halides stabilize {100} facets," J. Phys. Chem. Lett. **4**, 2209–2216 (2013).

[45]R. Jiang, H. Chen, L. Shao, Q. Li, and J. Wang, "Unraveling the evolution and nature of the plasmons in (Au core)-(Ag shell) nanorods," Adv. Mater. **24**, OP200–OP207 (2012).